Final Technical Report

Award Number	G19AP00030
Title of award	Rapid Characterization of First-Order complexity of Large Earthquakes

Author and Affiliation

> Zhongwen Zhan
> Seismological Laboratory
> Division of Geological and Planetary Sciences
> California Institute of Technology
> 1200 E. California Blvd., MC 252-21
> Pasadena, CA, 91125
> Phone (626) 395-6906; FAX (626) 564-0715
> zwzhan@gps.caltech.edu

Term covered by the award

> February 1st, 2019 to January 31, 2020

Abstract

One of the USGS NEIC's priorities is to characterize global large earthquakes accurately and timely, and to assess impacts due to ground shaking and secondary hazards. While for most large earthquakes current procedures/tools work well, in the last decade, we also witnessed many complex large earthquakes that are challenging to characterize. In particular, multiple faults may be involved in a single earthquake, and the directivity on individual faults strongly affects the distribution of shaking intensity. It is important to characterize these complex events timely and robustly for rapid hazard assessment and better understanding of long-term seismic hazard. In this project, we developed a modified subevent method as a bridge from point source solutions to better finite-fault models, to rapidly resolve first-order complexities of large events. In this method, earthquakes are parameterized as multiple point or Haskell sources, and 3D Green's functions are used in inversions to avoid artifacts caused by structural complexities. We implemented and applied this method to the 2018 Fiji Mw 8.2 and Mw 7.9 deep earthquake doublet, using mostly teleseismic waveforms. After the 2019 Mw 7.1 Ridgecrest earthquake, we expanded the method to include local and regional seismograms in the inversion, using 3D Green's functions generated with the Southern California Earthquake Center (SCEC) community velocity model (CVM). These results suggest that the subevent method, while not yet ready for fully automatic operations, can deliver rapid constraints on large earthquake ruptures using teleseismic and regional data.

Report

One of the priorities of the U.S. Geological Survey (USGS) National Earthquake Information Center (NEIC) is to characterize large global earthquakes accurately and rapidly, and to assess impacts due to ground shaking and secondary hazards (e.g., landslides, liquefaction). USGS and the entire seismology community have progressed tremendously in characterizing large earthquakes, especially since the 2004 Mw9.1 Sumatra earthquake, a wake-up call for all seismologists [Lay et al., 2005]. Once a large event is detected, its location, depth, origin time, and moment tensors are derived from multiple automated algorithms (e.g., USGS W-Phase and Body-Wave solutions, GlobalCMT solutions), which allow cross validation among different solutions. Next, to better characterize large events, we seek to constrain the finiteness of sources, such as rupture dimension, rupture speed, and slip distribution. Both USGS scientists (e.g., USGS finite-fault models by Gavin Hayes) and seismologists around the world participate in this step, using various methods and datasets [Ji et al., 2002; Ishii et al., 2005; Lay et al., 2010; Meng et al., 2012; Minson et al., 2013; Wei et al., 2013; Fan et al., 2016]. In finite-fault modeling, usually one of the nodal planes identified from moment tensor inversions is assumed to be the fault plane, and linearized or non-linear inversions are used to estimate spatiotemporal evolution of slip. Short-period back-projection is another method used to estimate finite source characteristics without pre-defining the fault planes, though this approach is not currently implemented at the USGS NEIC.

For most large earthquakes, this procedure works remarkably well. A good example is the 2015 Mw7.8 Nepal earthquake. Soon after the earthquake, USGS posted technical information about its moment tensor solutions and finite-fault models [Hayes et al., 2015], which both remain satisfactory long after the earthquakes when more detailed models and back-projection images are published [Avouac et al., 2015; Fan and Shearer, 2015; Galetzka et al., 2015; Wang and Fialko, 2015]. This capability proves critical for accurate prediction of strong ground motion and

assessment of damage in populated areas (ShakeMap and PAGER). These source parameters from USGS are also used in evaluating possible tsunami associated with submarine earthquakes.

However, in the last decade, we also witnessed complex large earthquakes, for which current procedures did not work so well. Some of the events have truly complex ruptures, such as multiple fault segments, variable rupture speed/directions, dynamic triggering, re-rupture of the same fault patches. This kind of events often poses significant challenges to current finite-fault modeling methods, which make various assumptions about ruptures (e.g., single fault, constant rupture speed, single rupture front growing outward from hypocenter, and/or smooth slip distribution). Complex events often have substantial non-double-couple components, which make the choice of fault planes difficult.

In the meanwhile, some other earthquakes appear more complex than what they actually are, due to structural effects. Large earthquakes concentrate in regions with probably the strongest lateral heterogeneities: plate boundaries between the oceanic and continental plates, steep topography/bathymetry, and deep sedimentary basins. However, almost all source-modeling methods assume relatively simple Green's functions. In earthquake short-period back-projection, the effective Green's functions are essentially delta functions shifted by corresponding travel times, without considering the free-surface effects (e.g., pP, sP). In most finite-fault inversions, homogeneous half-space or 1D layered Earth models are used so that depth phases and other simple reverberations are taken into account. However, 3D structures can distort direct seismic phases and produce strong secondary arrivals, which can be misinterpreted as source complexities.

While refining earthquake rupture models using new methods and more data is a never-ending exercise for seismologists, it is important to timely and robustly characterize these complex events for two reasons. (1) Rapid assessment of seismic hazard. For example, Wirth et al. [2017] simulated 50 different scenarios of Cascadia megathrust M9 earthquakes and found that the timing, locations, and directivity of the these subevents strongly controls distribution of strong ground motion in Seattle and nearby cities. (2) Better understanding of earthquake physics for long-term hazard assessment. Can and how likely are multiple faults to rupture in a single event? Only by identifying and detailed studies of truly complex events in the past we can answer this question better in the future. It is well known from geological and seismological data that large earthquakes often involve multiple asperities/subevents. The 2012 M8.6 Indian Ocean earthquake involved rupture on more than four faults. The USGS ShakeMap for the 2016 M7.8 Kaikōura earthquake is largely controlled by the 12 crustal faults involved, while the role of the megathrust fault is still being debated. More relevant to the seismic hazard in the United States, Goldfinger et al. [2003] and Wang et al. [2013] show that the 1700 Cascadia M9 megathrust earthquake may have at least four large asperities. Wirth et al. [2017] simulated 50 different scenarios of Cascadia megathrust M9 earthquakes and found that the timing, locations, and directivity of the high stress-drop subevents strongly controls distribution of strong ground motion.

With traditional source inversion methods, seismologists can determine the first order picture quickly and accurately for a garden-variety earthquake, but not earthquakes with such complexities. Nealy and Hayes [2015] developed a real-time double-point source method. However, they use long period (T>200s) W-Phase and can not resolve complexities for more than two subevents or at shorter period. For example, the 2018 M7.9 Gulf of Alaska earthquake was thought to have a simple EW-strike fault plane and slip concentrated at shallow depths. Months after the earthquake, the aftershocks start to reveal complex patterns along multiple

lineations, potentially seismogenic faults. If a similar earthquake happens closer to regions with high population density, it would be desirable to image this multi-fault rupture quickly to better evaluate ground motions.

Multiple subevent methods have been proposed in the past (Kikuchi and Kanamori, 1982; Tsai et al. (2005); Duputel et al., 2012; Zhan et al., (2014); Zhan and Kanamori, 2016; Duputel and Rivera, 2017). We propose a modified subevent method to rapidly resolve first-order complexities of large events. In this method, earthquakes are parameterized as multiple point or Haskell sources, which include radiation pattern and directivity effects. We use 3D Green's functions to avoid misinterpreting structural effects as complex ruptures. This new method aims to capture complex ruptures that are difficult to capture automatically in finite-fault inversions directly, such as changes in rupture direction or rupture speed, dynamic triggering of new subevents, and changes in subevent depth/focal mechanism. Important known source-side structures, such as topography, bathymetry, and/or basins will be taken into account when interpreting the observed waveforms, to avoid artifacts.

Application to the 2018 Fiji deep earthquake doublet

On August 19th, 2018, the first instrumentally recorded M>8 Fiji deep earthquake occurred (Fig. 1A), with a centroid depth of 556 km and a moment magnitude (Mw) 8.2, slightly smaller than the 1994 Bolivia Mw 8.2 earthquake, the second largest deep earthquake after the 2013 Okhotsk Mw 8.3 earthquake. The Mw 8.2 Fiji event produced hundreds of aftershocks, elevating seismic activity within a few hundred kilometers. On September 6th, a Mw 7.9 earthquake occurred about 250 km to the west at 655 km depth (Fig. 1A), being the second largest deep earthquake in the Fiji-Tonga region. Background seismicity in the Mw 7.9 source area had been minimal but increased substantially since the Mw 8.2 earthquake (Fig. 1B). Presumably, the Mw 8.2 event triggered the Mw 7.9, forming the first magnitude 8 (M8) deep earthquake doublet (Tibi et al., 2003; Ye et al., 2016).

We image the doublet rupture processes and dimensions by subevent inversions, using teleseismic P, SH, and pP waveforms. Furthermore, pP depth phases added to the inversion help resolve possible variations in subevent depths. In this method, we invert for the centroid locations, centroid times, durations, and moment tensors of all subevents. Our method combines non-linear inversion for a subset of parameters and linear inversion for the rest. We apply Markov Chain Monte Carlo (MCMC) method to sample the posterior Probability Density Functions (PDFs) of the nonlinear parameters including the timings, locations, and durations of subevents. For a given set of subevent timings, locations, and durations (i.e., one MCMC sample), we evaluate the apparent source time function for each station, and linearly invert the seismic data for the subevent moment tensors. The data misfit from the set of nonlinear parameters and the corresponding moment tensor solutions is then used to estimate the probability in the MCMC inversion. Compared with a fully non-linear inversion scheme, this hybrid approach requires much less computation to search the parameter space, hence provides more robust solutions. The number of subevents increases iteratively until the waveforms are fit well. More details of our subevent method can be found in the supplementary material.
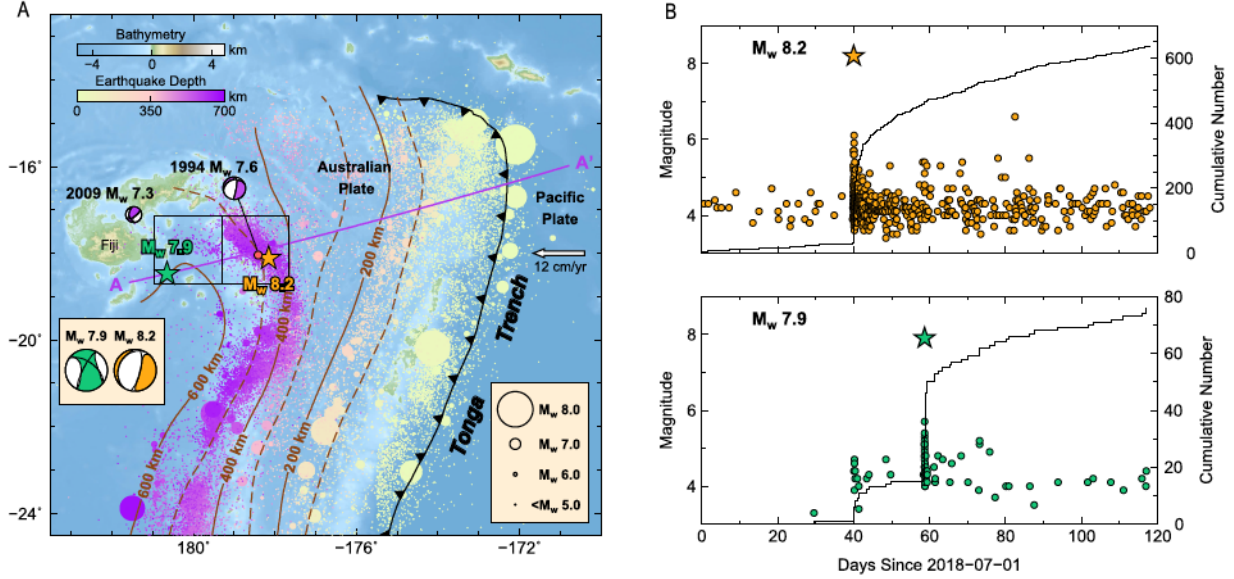
Fig. 1. Tectonic setting and seismicity. *(A) The 2018 Fiji deep earthquake doublet (Mw 8.2 and Mw 7.9) occurred in the northern end of Fiji-Tonga subduction zone where the Pacific plate subducts under the Australian plate, as illustrated by the background seismicity (dots) based on the ISC catalog and the slab depth contours from the Slab 2.0 model (Hayes et al., 2018). The stars show the mainshock epicenter locations, and the mainshock moment tensors are displayed in the inset. (B) Seismic activity around the Mw 8.2 and Mw 7.9 events in the yellow and green squares in (A) based on the ISC catalog. Body wave magnitudes are plotted except for the mainshocks. Solid black lines denote the cumulative number of aftershock in the mainshock regions (boxes in A). The Mw 8.2 event triggered hundreds of aftershocks near its rupture area and also elevated activity in the source region of the later Mw 7.9 event, during the three weeks in between. The Mw 7.9 event produced another tens of aftershocks around its rupture area.*

The subevent model for the M_w 8.2 earthquake (Fig. 2A) shows two stages of rupture. The first stage includes subevent E1 (centroid time τ_C=7.8 s, M_w 7.4), E2 (τ_C=10.7 s, M_w 7.8), and E3 (τ_C=12.3 s, M_w 7.6), aligned approximately in the NE direction with similar focal mechanisms (average strike/dip/rake=54°/83°/−76°, 174°/17°/−149°). Posterior Probability Density Functions (PDFs) of the subevent depths suggest that E3 is about 30 km shallower than E1 and E2, preferring the stage-1 rupture to be on the steep NE-strike fault plane (strike/dip=54°/83°), which is also supported by the nearly vertical band of aftershocks. The largest subevent of stage 1, E2, appears to have triggered large slip on multiple faults in stage 2. Subevents E4 (τ_C=14.4 s, M_w 7.8), E5 (τ_C=17.2 s, M_w 7.7) and E6 (τ_C=20.5 s, M_w 7.9) are aligned towards the northwest (NW) and they have relatively similar focal mechanisms (average strike/dip/rake=2°/72°/−96°, 201°/20°/−71°). The difference in radiation pattern between the two stages is evident on the teleseismic P-wave displacement seismograms with flipping polarities (Fig. 2B). Posterior PDFs suggest that E2, E4, E5, and E6 rupture sequentially towards shallower depths by about 30 km, rejecting the shallow west-dipping nodal plane (strike/dip=201°/20°) as the rupture plane. Furthermore, as E2, E4, E5, and E6 centroid locations are not aligned in the north-south (N-S) direction, it is also unlikely that they occurred on the N-S striking, steep fault plane (strike/dip=2°/72°). Therefore, we conclude that the stage-2 rupture must involve multiple faults, although the exact geometry is uncertain (e.g., en echelon vs. perpendicular faults). Previous magnitude 7 deep earthquakes in Fiji-Tonga show a diversity of fault geometries (Warren et al., 2007). The sum of the subevent moment tensors explains the long period moment tensor solution

of the M_w 8.2 earthquake well, including the ~10% non-double-couple (non-DC) component. The overall dimension of stage 2 is ~30 km, about the same as stage 1 but with much larger total moment, suggesting substantially higher stress drop in stage 2.

The M_w 7.9 event of the Fiji doublet has ~30% non-double-couple (non-DC) component in the USGS WPhase and the Global CMT solutions, compared with ~10% for the M_w 8.2 event. This large non-DC is reflected by the diverse subevent focal mechanisms we derived from waveforms (Fig. 2A), and supported by the deviation of polarity-based focal mechanism from the best-fitting double-couple of the Global CMT solution. The earthquake first ruptured to the east (E1-E2), then the major subevents (E3 to E6) occurred in a band from SW to NE direction (Fig. 2A). Given the uncertainty of subevent locations and focal mechanisms, it is unclear whether they ruptured on a single NE-strike fault plane or as a cascade of ruptures on multiple faults. The largest four subevents from E3 to E6 account for >90% of the total moment and are concentrated within 40 km from each other laterally (Fig. 2A) and vertically, comparable to the dimension of the M_w 8.2 event's stage 2 rupture.
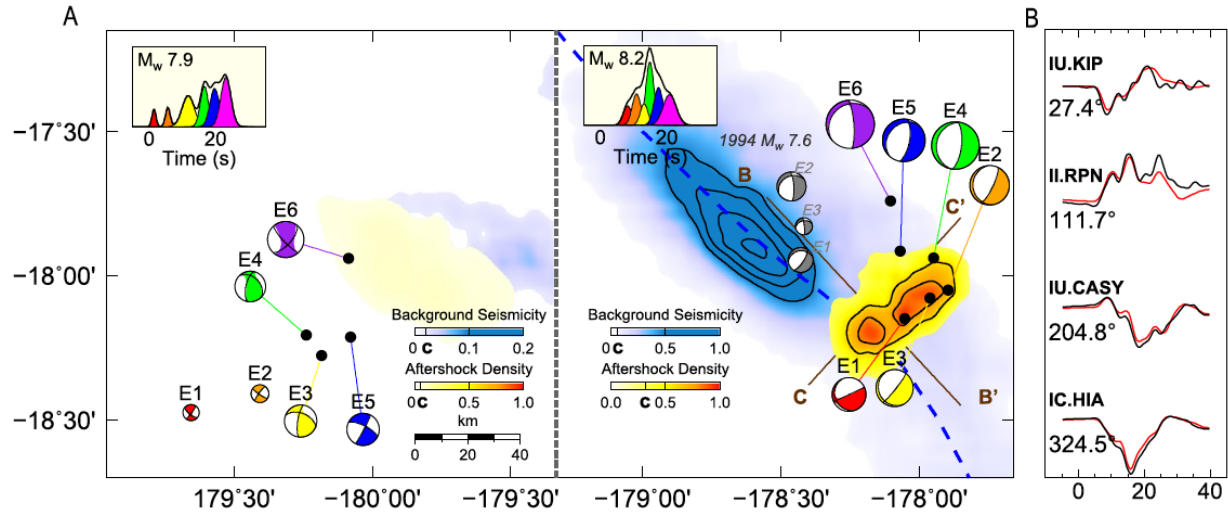

Fig. 2. Rupture processes of the 2018 Fiji doublet. *(A) Subevent models for the M_w 7.9 (left half) and the M_w 8.2 events (right half). The black dots are centroid locations of the subevents, whose moment rate functions (MRFs) are shown in the inset with the same colors as their moment tensor beach balls. Density contours of background seismicity and aftershocks are based on the USGS NEIC catalog, and displayed with different color scales and truncations ("C" on the colorbars if not 0). The M_w 8.2 event initiated near the slab center (blue dashed curve as inferred from the maximum background seismicity), but ruptured mostly 30 km to the NE by subevent E2, and E4-E6. Grey beachballs are subevent model of the 1994 Fiji M_w 7.6 earthquake. (B) Representative displacement waveform fits for the subevent model of the M_w 8.2 event at different azimuths, with data in black and synthetics in red. Early and late parts of the waveforms have opposite polarities at KIP and CASY, suggesting different focal mechanisms along the rupture.*

Application to the 2019 Ridgecrest M6.4 and M7.1 earthquakes

In July 2019, two powerful earthquakes (magnitude 6.4 and 7.1, respectively) occurred near the Ridgecrest, southern California (Fig. 3). The Ridgecrest earthquake sequence began on July 4th when a Mw 6.4 foreshock struck the Searles Valley, followed by a Mw 7.1 mainshock that occurred ~34 hours later. The Ridgecrest earthquake sequence occurred in the Little Lake and the Airport Lake fault zones, which are part of the Eastern California Shear Zone that accommodates ~20% deformation of Pacific-North America plate motion and has hosted several destructive earthquakes in the last few decades (Hauksson et al., 1995).
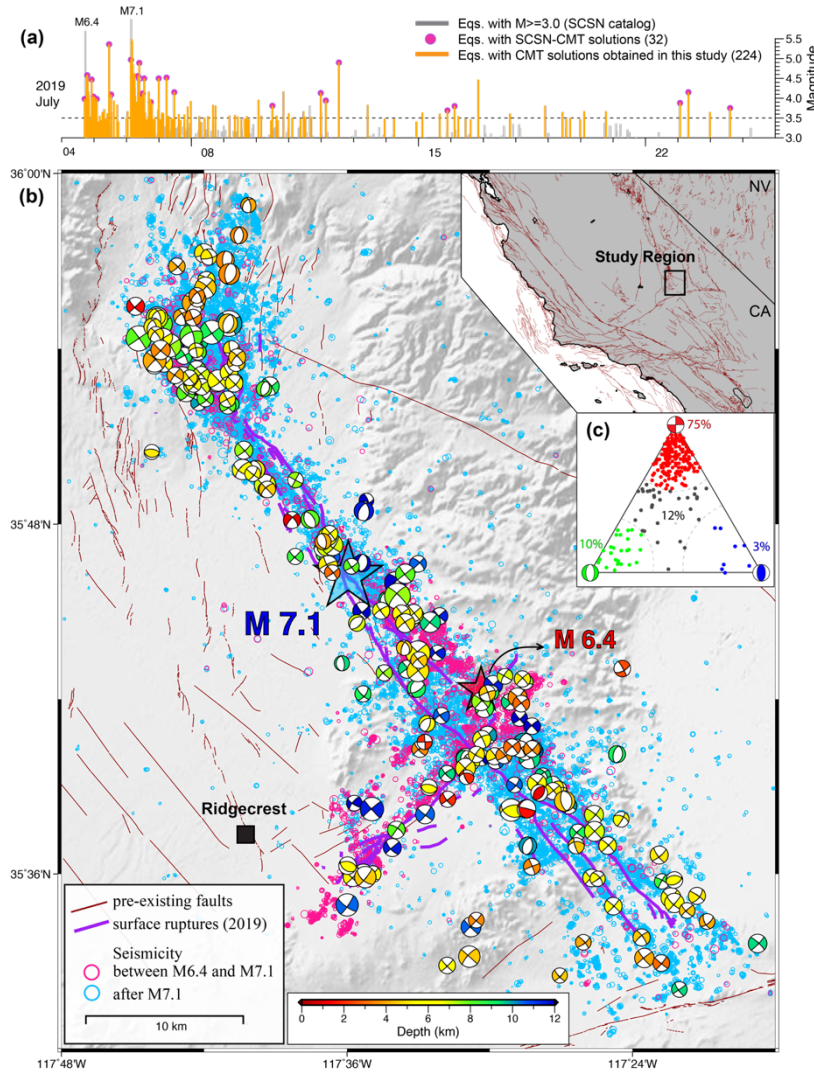
Fig. 3. Seismicity and regional tectonics in the Ridgecrest region. *(a) Aftershocks of the 2019 Ridgecrest sequence for the first 20 days after the M_w 6.4 event. Events that have the Southern California Seismic Network (SCSN) Centroid Moment Tensor (CMT) solutions are shown in purple circles, events with CMT solutions obtained in this study are colored in orange. The number in parentheses shows the number of CMT solutions in each catalog, indicating a more comprehensive catalog from our study. (b) Map showing the 2019 Ridgecrest sequence, where the aftershocks following the M_w 6.4 and M_w 7.1 event are shown as magenta and cyan dots, respectively. The purple lines show the surface ruptures during the 2019 Ridgecrest based on field mapping and satellite data (Brandenberg et al., 2019). The moment tensors obtained in this study are shown as beach balls, colored by focal depths. (c) Triangle diagram (Frohlich, 1992) shows that the aftershocks are dominated by strike-slip events.*

Here, we apply the subevent inversion method to estimate rupture process of the M_w 6.4 and M_w 7.1 earthquake sequence. We treat large earthquake as a series of subevents of varying location, timing and point source focal mechanism. This flexible yet simple source parameterization allows us to constrain first-order rupture complexity of large earthquakes robustly. In practice, we optimize some of the source parameters (locations, centroid times and durations) nonlinearly, while inverting for the rest of the source parameters (moment tensors) linearly. For the nonlinear parameters, we generate Markov chains with a Metropolis-Hasting algorithm, in which the proposal models are generated by sampling through one of the nonlinear parameters from their confidential distribution while keeping the other nonlinear parameters at their current values.

In each step of forward calculation, we linearly invert for the subevent moment tensors by extending the approach used by Minson and Dreger (2008) to multiple subevents. We generate 72 Markov Chains with random first samples, and finally keep the 24 best fitting chains, to eliminate the dependency of the inversion on the initial values. Subevent moment tensors are constrained to be deviatoric, with no isotropic components. We apply a bounded uniform prior probability density function for all non-linear parameters in the inversion. We also adopt a

penalty term to accommodate the moment-duration scaling relationship observed for large earthquakes (Meier et al., 2017) by rejecting models of extremely sharp or flat source time functions. We set the data error to be 10% of the final misfit with the optimal models; the true data errors of seismograms are trivial, but additional errors may be introduced due to nonlinear wave propagation effects (e.g. inaccurate velocity model).

We use teleseismic (epicentral distances from 30 to 90 degrees) P wave records of 33 stations, teleseismic SH wave records of 39 stations, regional (epicentral distances from 50 to 150 km) Rayleigh waves of 31 stations and regional Love waves of 30 stations. The data are selected from all available Global Seismic Network broadband stations and the Southern California Earthquake Data Center strong motion stations for good quality and azimuthal coverage. We remove the instrument response and linear trends of the waveforms, and rotate the two horizontal components to the radial and transverse components. We apply filter bands of 0.01-0.2 Hz for teleseismic body waves and 0.02-0.2 Hz for regional surface waves, and allow time shifts up to 2.0 s for P waves and 5.0 s for SH and surface waves to account for path complexities and picking errors. The calculation of Green's functions is based on the propagator matrix method with plane wave approximation for the teleseismic body waves, and the frequency-wavenumber integration method for regional surface waves. The source side velocity model is based on a combination of a 4-layer 1D elastic model and iasp91 model. We start with one subevent and iteratively increase the number of subevents until the main features of the waveform are well fitted and the sum of subevent moments agrees with the long period moment.

The aftershock locations and the InSAR interferograms illuminate the geometry of the faults, which provide important constraints on our subevent models. For the M 6.4 event, we anchor the location of the third subevent by the maximum surface offset on the NE-SW trending conjugate fault observed from the unwrapped interferograms, while the first and second subevents are allowed to move freely in the whole space. For the M 7.1 event, we fix the first subevent at the hypocenter, and search for the locations of other subevents along a NW-SE trending plane derived from the surface rupture and aftershocks.

On the basis of kinematic subevent inversion of seismograms from the dense regional seismic network and global seismic stations, the Mw 6.4 earthquake had a duration of about 12 s, with three subevents best explaining the data (Fig. 4). These three subevents coincide with at least three faults. The 6-km-long northwest-trending fault slipped first, with an equivalent Mw 6.1 (subevent E1). This is consistent with the hypocenter of this event, which is located about 2 km northwest of the long southwest trending fault. Thus, a rupture propagated over a short southwest-trending fault with only about 5 km of surface break, yet the equivalent magnitude for this segment, was the Mw 6.2 subevent (E2). Our analysis of this subevent indicates that it is required by the data and that the magnitude is well resolved. However, this subevent may also include slip on an adjacent northwest-trending orthogonal fault. Because the seismicity on the E2 segment extends across the main fault of the mainshock (Fig. 2), part of the slip probably occurred on the other side, but only at depth. The rupture then jumped to a larger southwest-trending fault that is about 15 km long, producing again an equivalent seismic moment to an Mw 6.2 earthquake (E3) and a large surface rupture.

Our kinematic subevent model of the Mw 7.1 mainshock shows that the rupture lasted for about 22 s and can be explained by four subevents (Fig. 4). The initial 5 s of the rupture had little moment, whereas the subevent with the largest moment (subevent E1, Mw 6.9) occurred close to the hypocenter between 5 and 10 s. This subevent appears to have ruptured bilaterally, given its large seismic moment. Centroid locations of the later subevents propagated very slowly to the

southeast, suggesting a unilateral rupture. The final subevent, E4 (at 20 s), occurred ~25 km southeast of the first subevent E1 (at 7 s), indicating a slow average rupture velocity of roughly 2 km/s.
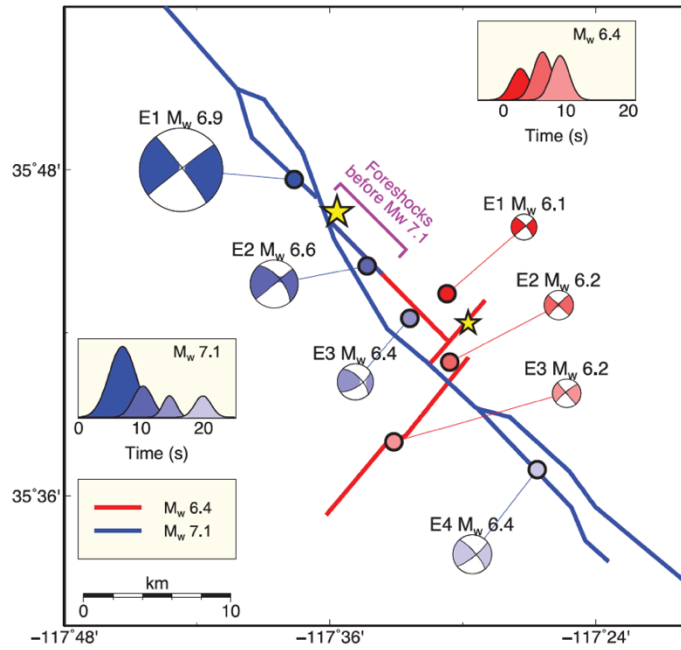
Fig. 4 Kinematic summary of rupture processes. *The M_w 6.4 foreshock ruptured three main faults. This event was followed by foreshock activity along a northwest-trending fault and eventually triggered the M_w 7.1 event. The mainshock had four main subevents and ruptured bilaterally. Both events have very slow rupture velocities of ~2 km/s.*
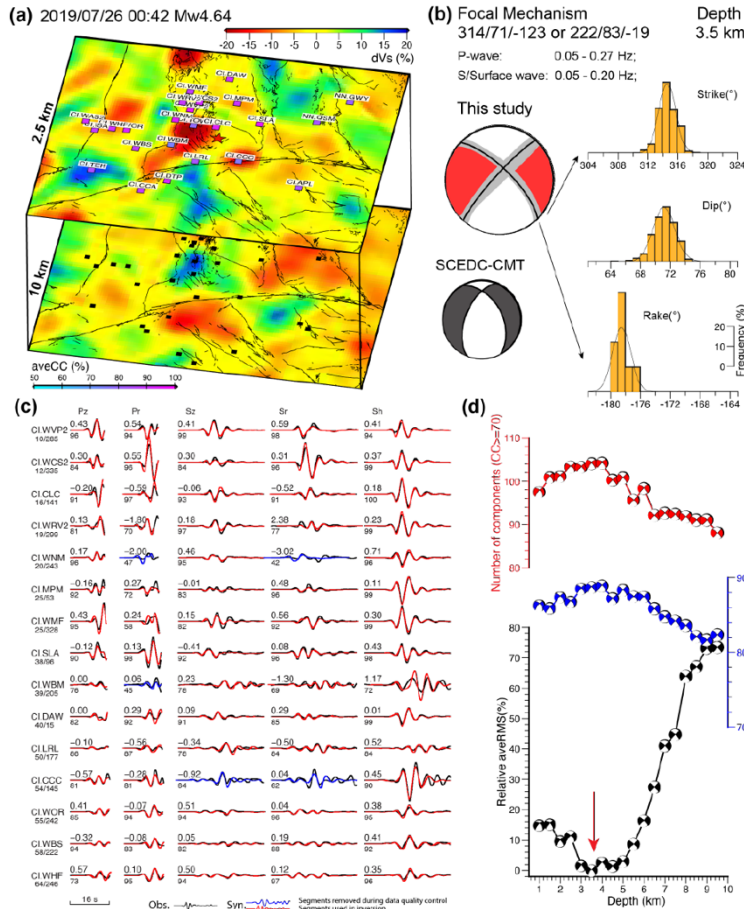
Figure 5. Source parameters inversion results for the 2019/07/26 00:42 M4.6 event. *(a) The earthquake location (red star) and seismic stations (squares) used in this study. The stations are colored by the averaged waveform cross-correlation coefficients (CC), which serve as proxies for the quality of inversion. The background color shows the Southern California Earthquake Center (SCEC) 3D community velocity model (CVM) of CVM-S4.26 (Lee et al., 2014), highlighting the complicated 3D velocity structures in the region. (b) The optimal double couple solutions, inversion parameters, and the associated uncertainties. For comparison, the focal mechanism solution from the Southern California Seismic Network (SCSN) Centroid Moment Tensor (CMT) catalog is shown as the black beachball. (c) Waveform fitting at representative stations. The black and red lines indicate data and synthetics, respectively. The blue lines represent the waveforms discarded in our automatic data selection. The station names are indicated on the left of waveform pairs along with the distance in km and azimuth in degree. The waveform CC (lower) and time-shits (upper) are shown around the waveform pairs. (d) The averaged CC, the number of segments with CC larger than the threshold of CC, and the waveform misfit as a function of focal depth and focal mechanism, indicating a well-resolved focal depth of 3.5 km.*

9

The Ridgecrest region is located within the Basin and Range Providence with strong 3D velocity heterogeneities (Black et al., 2002; Lee et al., 2014) (Fig. 5a). The existence of these 3D heterogeneities will evitable modify the arriving time and shape of waveforms. Thus, the inversion based on a simplified 1D velocity model may introduce large uncertainties in moment tensor solutions (Wang & Zhan, 2019). In this project, we take into account the Southern California Earthquake Center (SCEC) 3D Community Velocity Model (CVM) in source inversion to study the rupture processes. As a demonstration, Figure 5 shows an inversion of aftershock focal mechanisms using the 3D CVM. The result is substantially different from that derived from a 1D SoCal model, from the SCEDC moment tensor catalog. We are in the processing of applying the 3D Green's functions in the kinematic inversion of mainshock ruptures.

Summary

As proposed, we have successfully implemented a new subevent method and enhanced it with a few new capabilities: (1) joint inversion of multiple data types, including but not limited to teleseismic body waves, local and regional strong motion data; (2) usage of 3D Green's functions that help reduce inversion artifacts; (3) Bayesian inverse approach that can provide some insights on the model uncertainties. Our application of the new method to the 2018 Fiji deep earthquake doublet and the 2019 Ridgecrest M6.4 and M7.1 mainshocks demonstrated the effectiveness of the new method. In particular, we reveal complicated rupture processes in both earthquakes, involving multiple fault planes, changing focal mechanisms, and/or possible dynamic triggering during ruptures. We believe it is valuable to continue the development of the subevent method, in order to (1) make it an semi-automatic operation tool, (2) include geodetic data in the inversions for large earthquakes on land, and (3) feed the subevent model to finite-fault inversions to guide the choice of fault planes and kinematic parameters. Together this should lead to a complete set of models to describe large earthquakes in different levels of complexity.

Project data: There is no data generated by this project. All data used are downloaded from the Incorporated Research Institutions of Seismology (IRIS).

Bibliography of all publications resulting from the work performed under the award.

Ross, Z.E., Idini, B., Jia, Z., Stephenson, O.L., Zhong, M., Wang, X., Zhan, Z., Simons, M., Fielding, E.J., Yun, S.H. and Hauksson, E., 2019. Hierarchical interlocked orthogonal faulting in the 2019 Ridgecrest earthquake sequence. Science, 366(6463), pp.346-351.

Jia, Z., Shen, Z., Zhan, Z., Li, C., Peng, Z. and Gurnis, M., 2020. The 2018 Fiji Mw 8.2 and 7.9 deep earthquakes: One doublet in two slabs. Earth and Planetary Science Letters, 531, p.115997.

Wang, X. and Z. Zhan, 2020. Seismotectonics and fault geometries of the 2019 Ridgecrest sequence: insight from aftershock moment tensor catalog using 3D Green's functions. Under review by Journal of Geophysical Research, Solid Earth.

Meeting Abstracts

Jia, Z.,Wang, X., & Zhan, Z. (2019). Geometrically complex rupture processes of the 2019 M6. 4 and M7. 1 Ridgecrest sequence. Presented at the AGU Fall Meeting 2019, AGU.

Wang, X. and Zhan, Z., 2019. Fault geometry of the 2019 Ridgecrest sequence: insight from aftershock moment tensor catalog using 3D Green's functions. AGUFM, 2019, pp.S31F-0478.

References

Avouac, J.-P., L. Meng, S. Wei, T. Wang, and J.-P. Ampuero (2015), Lower edge of locked Main Himalayan Thrust unzipped by the 2015 Gorkha earthquake, Nature Geoscience, 8(9), 708-711.

Brandenberg, S.J., Wang, P., Nweke, C.C., Hudson, K., Mazzoni, S., Bozorgnia, Y., Hudnut, K.W., Davis, C.A., Ahdi, S.K., Zareian, F. and Fayaz, J., 2019. Preliminary report on engineering and geological effects of the July 2019 Ridgecrest earthquake sequence (pp. 1-69). Geotechnical Extreme Event Reconnaissance Association.

Black, R. A., Walker, J. D., & Baker, G. S. (2002). Three-dimensional gravity modeling and crustal-density variations, Panamint Range to the eastern Sierra Nevada, southeastern California. In A. F. Glazner, J. D. Walker, & J. M. Bartley (Eds.), Geologic Evolution of the Mojave Desert and Southwestern Basin and Range (Vol. 195, p. 0). Geological Society of America. https://doi.org/10.1130/0-8137-1195-9.229

Duputel, Z., H. Kanamori, V. C. Tsai, L. Rivera, L. Meng, J.-P. Ampuero, and J. M. Stock (2012), The 2012 Sumatra great earthquake sequence, Earth and Planetary Science Letters, 351, 247-257.

Duputel, Z., and L. Rivera (2017), Long-period analysis of the 2016 Kaikoura earthquake, Physics of the Earth and Planetary Interiors, 265, 62-66, doi:10.1016/j.pepi.2017.02.004.

Fan, W., and P. M. Shearer (2015), Detailed rupture imaging of the 25 April 2015 Nepal earthquake using teleseismic P waves, Geophysical Research Letters, 42(14), 5744-5752.

Fan, W., and P. M. Shearer (2016), Local near instantaneously dynamically triggered aftershocks of large earthquakes, Science, 353(6304), 1133-1136.

Galetzka, J., D. Melgar, J. F. Genrich, J. Geng, S. Owen, E. O. Lindsey, X. Xu, Y. Bock, J.-P. Avouac, and L. B. Adhikari (2015), Slip pulse and resonance of the Kathmandu basin during the 2015 Gorkha earthquake, Nepal, Science, 349(6252), 1091-1095.

Goldfinger, C., C. H. Nelson, J. E. Johnson, and S. S. Party (2003), Holocene earthquake records from the Cascadia subduction zone and northern San Andreas fault based on precise dating of offshore turbidites, Annual Review of Earth and Planetary Sciences, 31(1), 555-577.

Hauksson, E., Hutton, K., Kanamori, H., Jones, L., Mori, J., Hough, S. and Roquemore, G., 1995. Preliminary report on the 1995 Ridgecrest earthquake sequence in eastern California. Seismological Research Letters, 66(6), pp.54-60.

Hayes, G.P., Moore, G.L., Portner, D.E., Hearne, M., Flamme, H., Furtney, M. and Smoczyk, G.M., 2018. Slab2, a comprehensive subduction zone geometry model. Science, 362(6410), pp.58-61.

Hayes, G. P., R. W. Briggs, W. D. Barnhart, W. L. Yeck, D. E. McNamara, D. J. Wald, J. L. Nealy, H. M. Benz, R. D. Gold, and K. S. Jaiswal (2015), Rapid characterization of the 2015 Mw 7.8 Gorkha, Nepal, earthquake sequence and its seismotectonic context, Seismological Research Letters, 86(6), 1557-1567.

Ishii, M., P. M. Shearer, H. Houston, and J. E. Vidale (2005), Extent, duration and speed of the 2004 Sumatra–Andaman earthquake imaged by the Hi-Net array, Nature, 435(7044), 933-936.

Ji, C., D. J. Wald, and D. V. Helmberger (2002), Source description of the 1999 Hector Mine, California, earthquake, part I: Wavelet domain inversion theory and resolution analysis, Bulletin of the Seismological Society of America, 92(4), 1192-1207.

Kikuchi, M., and H. Kanamori (1982), Inversion of complex body waves, Bulletin of the Seismological Society of America, 72(2), 491-506.

Lee, E.-J., Chen, P., Jordan, T. H., Maechling, P. B., Denolle, M. A., & Beroza, G. C. (2014). Full‐3‐D tomography for crustal structure in southern California based on the scattering‐integral and the adjoint‐wavefield methods. Journal of Geophysical Research: Solid Earth, 119(8), 6421–6451.

Lay, T., C. J. Ammon, H. Kanamori, L. Rivera, K. D. Koper, and A. R. Hutko (2010), The 2009 Samoa-Tonga great earthquake triggered doublet, Nature, 466(7309), 964-968, doi:10.1038/nature09214.

Lay, T., H. Kanamori, C. J. Ammon, M. Nettles, S. N. Ward, R. C. Aster, S. L. Beck, S. L. Bilek, M. R. Brudzinski, and R. Butler (2005), The great Sumatra-Andaman earthquake of 26 december 2004, Science, 308(5725), 1127-1133.

Meier, M.-A., J. P. Ampuero, T. H. Heaton, The hidden simplicity of subduction megathrust earthquakes. Science. 357, 1277–1281 (2017).

Meng, L., J.-P. Ampuero, J. Stock, Z. Duputel, Y. Luo, and V. Tsai (2012), Earthquake in a maze: Compressional rupture branching during the 2012 Mw 8.6 Sumatra earthquake, Science, 337(6095), 724-726.

Minson, S. E., and D. S. Dreger, Stable inversions for complete moment tensors. Geophys. J. Int. 174, 585–592 (2008).

Minson, S., M. Simons, and J. Beck (2013), Bayesian inversion for finite fault earthquake source models I—Theory and algorithm, Geophysical Journal International, 194(3), 1701-1726.

Nealy, J. L., and G. P. Hayes (2015), Double point source W-phase inversion: Real-time implementation and automated model selection, Physics of the Earth and Planetary Interiors, 249, 68-81.

Tsai, V. C., M. Nettles, G. Ekström, and A. M. Dziewonski (2005), Multiple CMT source analysis of the 2004 Sumatra earthquake, Geophysical Research Letters, 32(17).

Tibi, R., Wiens, D.A., Inoue, H., 2003. Remote triggering of deep earthquakes in the 2002 Tonga sequences. Nature, 424, 921–925.

Wang, K., and Y. Fialko (2015), Slip model of the 2015 Mw 7.8 Gorkha (Nepal) earthquake from inversions of ALOS‐2 and GPS data, Geophysical Research Letters, 42(18), 7452-7458.

Wang, P. L., S. E. Engelhart, K. Wang, A. D. Hawkes, B. P. Horton, A. R. Nelson, and R. C. Witter (2013), Heterogeneous rupture in the great Cascadia earthquake of 1700 inferred from coastal subsidence estimates, Journal of Geophysical Research: Solid Earth, 118(5), 2460-2473.

Wang, X., & Zhan, Z. (2019). Moving from 1D to 3D velocity model: automated waveform-based earthquake moment tensor inversion in the Los Angeles region. Geophysical Journal International. https://doi.org/10.1093/gji/ggz435

Warren, L.M., Hughes, A.N., Silver, P.G., 2007. Earthquake mechanics and deformation in the Tonga-Kermadec subduction zone from fault plane orientations of intermediate-and deep-focus earthquakes. J. Geophys. Res., Solid Earth112, B5.

Wei, S., D. Helmberger, and J.-P. Avouac (2013), Modeling the 2012 Wharton basin earthquakes off-Sumatra: Complete lithospheric failure, Journal of Geophysical Research: Solid Earth, 118(7), 3592-3609, doi:10.1002/jgrb.50267.

Wirth, E., A. Frankel, J. Vidale, N. A. Marafi, and W. J. Stephenson (2017), 3-D simulations of M9 earthquakes on the Cascadia Megathrust: Key parameters and uncertainty, paper presented at AGU Fall meeting, New Orleans.

Ye, L., T. Lay, Z. Zhan, H. Kanamori, and J.-L. Hao (2016), The isolated~ 680 km deep 30 May 2015 M W 7.9 Ogasawara (Bonin) Islands earthquake, Earth and Planetary Science Letters, 433, 169-179.

Zhan, Z., and H. Kanamori (2016), Recurring large deep earthquakes in Hindu Kush driven by a sinking slab, Geophysical Research Letters, 43(14), 7433-7441.

Zhan, Z., H. Kanamori, V. C. Tsai, D. V. Helmberger, and S. Wei (2014), Rupture complexity of the 1994 Bolivia and 2013 Sea of Okhotsk deep earthquakes, Earth and Planetary Science Letters, 385, 89-96.